SEM characterization of surface metrology of rough ice at the mesoscale

Nicholas Butterfield[1], Penny M. Rowe[2,3], Emily Stewart[1], David Roesel[4], and Steven Neshyba[1,*]

[1]University of Puget Sound, 1500 N. Warner, Tacoma, Washington, USA
[2]Universidad de Santiago de Chile, Ave Bernardo O'Higgins 3363, Santiago, Chile
[3]NorthWest Research Associates, Redmond, Washington, USA
[4]Faculty of Nuclear Sciences and Physical Engineering, Czech Technical University in Prague, Břehová 7, 11519 Praha 1, Czech Republic

*Corresponding author: Steven Neshyba (nesh@pugetsound.edu)

Key Points:

- We discover a novel functional form for expressing backscattered electron intensity as a function of ice facet orientation.
- Gauss-Newton/Bayesian inversion robustly and flexibly yields three-dimensional mesoscale morphology.
- Surface roughness statistics are found to be sensitive not only to the degree of roughening, but also to its symmetry.

Abstract

We present a method for inferring surface morphology of ice from scanning electron microscope images. We first develop a novel functional form for the backscattered electron intensity as a function of ice facet orientation; this form is parameterized using smooth ice facets of known orientation. Three-dimensional representations of rough surfaces are retrieved at approximately micrometer resolution using Gauss-Newton inversion within a Bayesian framework. Statistical analysis of the resulting datasets permit characterization of ice surface roughness with a much higher statistical confidence than previously. A survey of results in the range -39℃ to -29℃ shows that characteristics of the roughness (e.g., Weibull parameters) are sensitive not only to the degree of roughening, but also to its symmetry. These results suggest that roughening characteristics obtained by remote sensing of atmospheric ice clouds can potentially provide more facet-specific information than has previously been appreciated.

1 Introduction

Cirrus clouds play an important role in the earth's climate by absorbing and reflecting infrared and solar radiation [*Stephens et al.*, 1990; *Lynch*, 2002; *Baran*, 2009, 2012, 2015]. The roughness of ice crystals in cirrus clouds affects this radiative balance, and also plays a role in remote sensing experiments [*Xie*, 2012; *Ulanowski et al.*, 2014; *Geogdzhayev and van Diedenhoven*, 2016; *Hioki et al.*, 2016]. Underlying these complex radiative interactions are individual, single-crystal processes, about which fundamental questions remain. Is there a difference, for example, between roughness associated with ice growth vs ablation? Is roughness facet-specific? To what extent do these differences influence remote sensing signals or atmospheric radiative transfer?

To address these questions, directly examining individual ice crystals in controlled laboratory experiments is a useful approach; our ability to obtain direct measurements of roughness statistics of ice crystals can "help constrain optical models for climate models or radiative closure studies" [*van Diedenhoven et al.*, 2016]. Indeed, recent years have seen considerable progress along these lines. In particular, investigations using scanning electron microscopy have shown that roughness can span multiple spatial scales [*Magee*, 2015; *Bancroft et al.*, 2016], and can be distinctly azimuthally anisotropic [*Pfalzgraff et al.*, 2010].

Nevertheless, our understanding of ice crystal roughness remains unsatisfactory. While roughening on prismatic facets has been characterized quantitatively by examining the structure of facet intersections (because roughness is more easily detected there), quantification of roughness at facet interiors has so far proven elusive. A methodology to infer fully three-dimensional morphology across broad regions of an ice facet, at scanning electron microscope resolution, would have distinct advantages for quantifying ice roughness.

Here, we present such a methodology. The method uses Gauss-Newton inversion of scanning electron images of ice, within a Bayesian framework, to retrieve three-dimensional morphologies of the ice surface. This inversion (henceforth "GNBF inversion"; see [*Rodgers*, 2000]) is applied in such a way that contiguity of surface height is an integral part of the algorithm, a feature that greatly suppresses effects of noise. Combined with the fact that these retrievals produce large datasets of surface heights over a two-dimensional surface, the ensuing statistical analyses are more robust than has previously been possible.

This paper is organized as follows. Section 2 describes scanning electron microscopy and imaging methodologies. A methodology for instrument calibration, and an algorithm for retrieving ice roughness topography, are central results of the paper; these are developed in Sections 3.1 and 3.2. In Section 3.3 we present retrieved scattering roughness, including roughness statistics. Sections 4 and 5 provide discussion and conclusions.

2 Methods

2.1 SEM imaging of ice

A Hitachi S-3400N VPSEM (henceforth "SEM") equipped with a backscattered electron detector and a Deben Ultra-Cool stage MK3 version Peltier cooling element is used to collect Scanning Electron Micrographs, using a protocol similar to that described by the authors in previous papers (e.g., [*Pfalzgraff et al.*, 2010; *Neshyba et al.*, 2013]). In all experiments, an accelerating voltage of 17 kV and a probe current of 70 μA are used. The typical experimental procedure is as follows. The specimen stub, made of rough-cut copper, is mounted on the room-temperature cooling element. A few milliliters of deionized water are frozen and cooled to -15 °C in an aluminum reservoir. The reservoir is placed in the chamber, and the chamber is closed and pumped down to a nominal operating pressure of 50 Pa, which corresponds to an ice-vapor equilibrium temperature of -32 °C. The temperature of the Peltier cooling element is then reduced to -31 °C and the specimen stub is allowed to equilibrate with the cooling element. The temperature is then slowly lowered to -39 °C at a rate of 0.5 °C per minute. This slow rate of cooling prevents crystals from preferentially freezing to the cold stage background and increases the quantity of viable crystals growing on the copper stub. At this temperature, crystals grow quickly and appear to present smooth, prismatic facets. Once several suitable hexagonal crystals are located and imaged for calibration, the temperature is increased to -33 °C or above. Further images of the same crystals are then acquired as they develop rough surfaces.

The SEM detector geometry is such that four backscattered electron detectors are positioned symmetrically around the electron beam source; each detector occupies a quadrant of an annular disk (Fig. 2.1a). The internal radius is 2 mm and the external radius is 7 mm. The backscatter detector assembly is approximately 10 mm above the sample during imaging. The source passes through the midpoint of the detectors and scatters from the substrate surface. Using Hitachi's 3D Acquisition Mode, returning electrons are captured by each detector independently at an interval of approximately four seconds per image, producing four near-simultaneous images of the surface. These images consist of pixels measuring $\sim 1 \mu m$ across (depending on magnification), whose values are given in backscatter intensity units (BIU) in the range 0 (black) to 255 (white). As can be seen by the brightness variation in Fig. 2.1, detectors A and C are most sensitive to variations in tilt angles in the *x*-direction, while B and D detectors are most sensitive to variations in the *y*-direction. The dependence of backscattered intensity as a function of facet orientation is a critical part of our development, and is described in Section 3.1. Next, we review formalism related to roughness distributions.

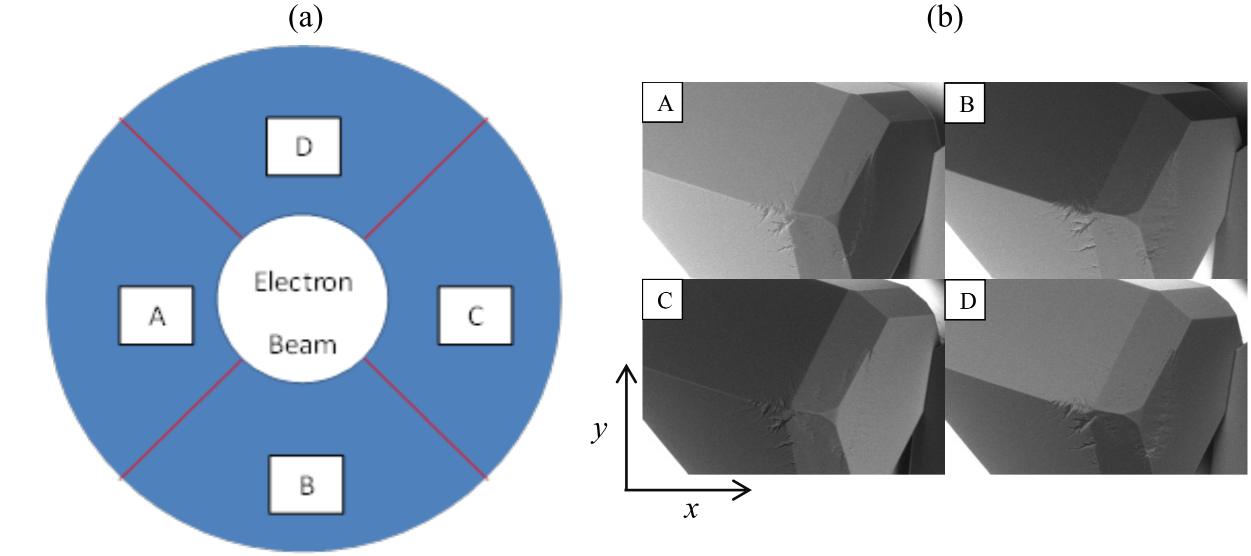

Figure 2.1 (a) Schematic of an SEM backscatter detector assembly. The electron beam passes through the center of the disk, and each detector occupies the quadrant indicated. (b) Near-simultaneous images of an ice crystal as recorded by each detector.

2.2 Roughness distribution analysis

The surface normal roughness value, *r*, defined in [*Neshyba et al.*, 2013] but here extended to two surface directions, is given by

$$r = 1 - \left(\frac{1}{1 + \left(\frac{dz}{dx}\right)^2 + \left(\frac{dz}{dy}\right)^2} \right)^{\frac{1}{2}}. \tag{2.1}$$

where the surface height, *z*, is understood to be a function of spatial dimensions *x* and *y*. Each microsurface (pixel) in a given surface is therefore assigned a value of r. A roughness value of zero indicates a pixel that is coplanar with a reference plane. This reference frame is obtained by a bilinear fit to any given retrieved surface segment, typically spanning 50×50 pixels or more, which is judged to be large compared the roughness scale. For statistical analysis, the resulting r-values are binned in intervals of ~0.01, and the resulting accumulations plotted as normalized probability density functions (PDFs). These PDFs are compared to two-parameter Weibull functions of the form

$$\rho(r) = \frac{2\eta}{\sigma^2 \mu^3} \left(\frac{\mu^{-2} - 1}{\sigma^2} \right)^{\eta - 1} \left(e^{-\left(\frac{\mu^{-2} - 1}{\sigma^2} \right)^{\eta}} \right) \tag{2.2}$$

where $\mu = 1 - r$, and σ is the standard deviation in r. The value of σ obtained this way is equivalent to the roughness parameter used by other authors, e.g., [*Shcherbakov et al.*, 2006a, 2006b; *Magee et al.*, 2014]. Regarding the shape parameter, when $\eta = 1$, the Weibull function reduces to the Cox-Munk function. Lower values of η produce more pronounced peaks close to $r = 0$ and a slower tail-off at higher r values. The best value for η is estimated by visual comparison to Weibull PDFs with a range of η.

3 Results

3.1 Characterization of SEM response to ice surface topography

To determine the three-dimensional structure of an object such as an ice crystal from SEM images, it is necessary to know how the local surface topography of a material relates to the backscattered electron signal recorded at detectors $A - D$. Based on the light-scattering model presented in Blinn [1977], we predicted that this response would depend on projections $\vec{n} \cdot \vec{b}$ and $\vec{n} \cdot \vec{d_I}$, where $\vec{n}$ is a surface normal vector, $\vec{d}_I$ points from the surface to detector I, and $\vec{b}$ is the beam vector (see Fig. 3.1).

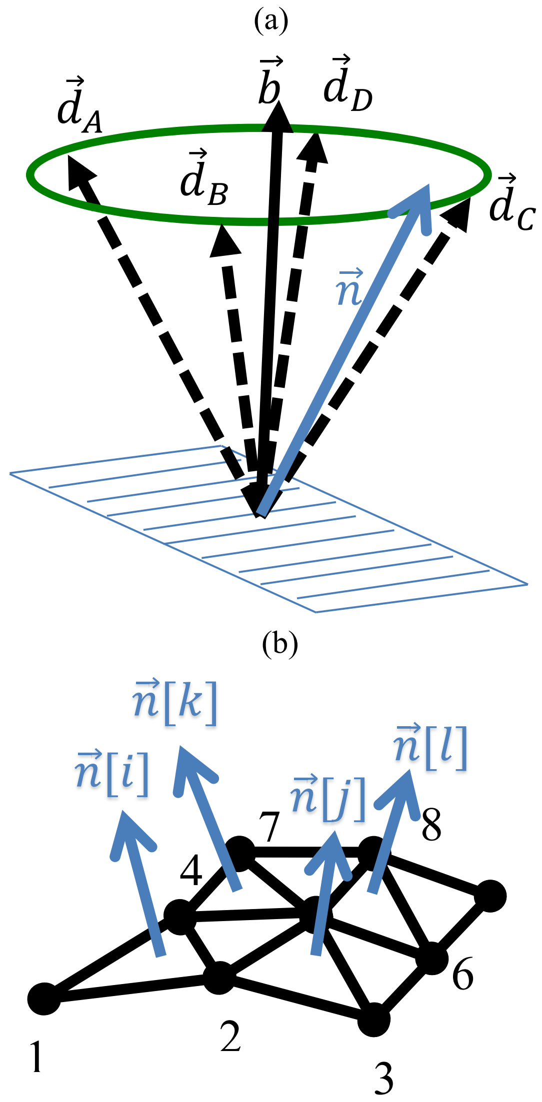

Figure 3.1. Vectors pertaining to the geometry of the stage. Detector and beam source vectors ($\vec{d}_I$ and $\vec{b}$) have unit length, while the surface normal ($\vec{n}$) is defined to have components $(N_x, N_y, 1)$.

We therefore examined the dependence of backscattered intensity on these projections. For the crystal shown in the inset to Fig. 3.2, for example, we identified prismatic facets **a** and **b**, and drew projected vectors $\vec{a}$, $\vec{b}$, and $\vec{c}$ (the latter corresponding to the crystallographic c-axis). These vectors were then used to compute a true (three-dimensional) surface normal vector, $\vec{n}$, for each facet, by a procedure described in Appendix A1. Projections $\vec{n} \cdot \vec{d}_I$ and $\vec{n} \cdot \vec{b}$ were computed for each facet/detector combination, and the backscattered intensities recorded. This process was repeated over a series of micrographs taken in 5° increments from 0° to 15° stage tilt angles. Examination of the resulting dataset showed that nearly all the variability in backscattered intensity depended on the *difference* between projections, $\vec{n} \cdot \left(\vec{d}_I - \vec{b}\right)$. Therefore, we define a *backscattered intensity response variable*,

$$s_I = \frac{1}{|\vec{n}|}\vec{n} \cdot \left(\vec{d}_I - \vec{b}\right) \qquad (3.1)$$

and graph the resulting locus of points, Fig. 3.2. The figure suggests a linear dependence,

$$F_I(s_I) = m_I s_I + b_I \qquad (3.2)$$

where I specifies a detector (*A-D*). Parameters m_I and b_I are therefore empirical parameters determined for any given crystal. From a physical standpoint, b_I may be thought of as a background brightness, and m_I a sensitivity. F_I, like c_I, is given in BIU, defined above.

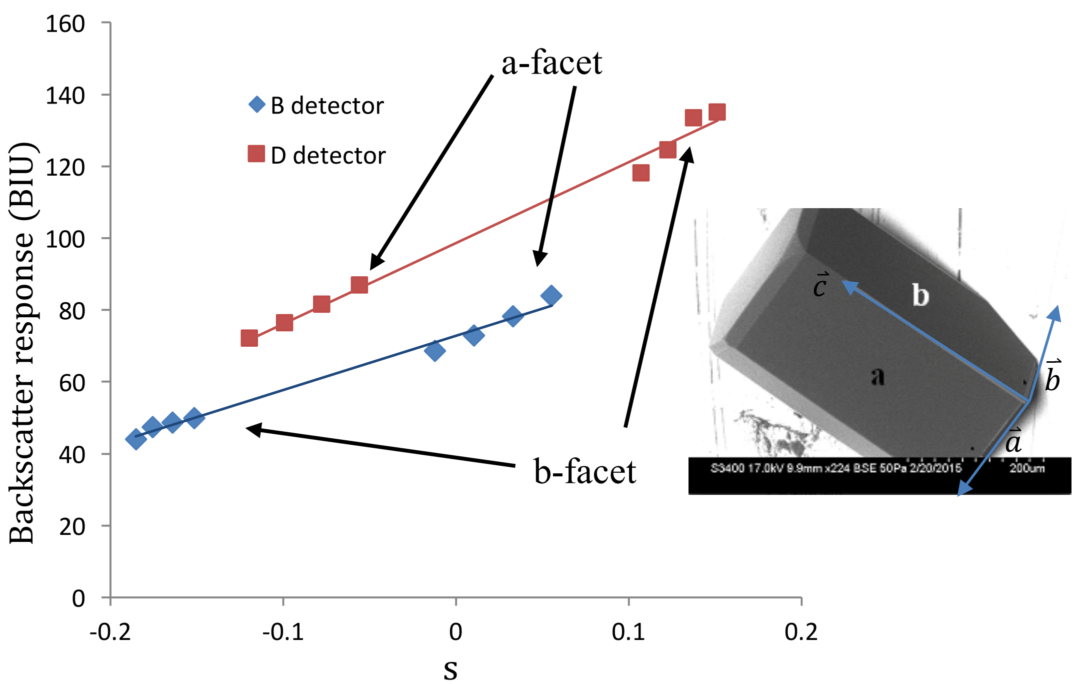

Figure 3.2. Examination of backscatter intensity dependence on the response variable, s_I. The corresponding crystal is shown in the inset, at an initial orientation of the SEM imaging stage; the stage was subsequently tilted along the horizontal axis by 5°, 10°, and 15° to obtain a total of four points for each facet/detector combination. Linear best fits yield parameters m_I and b_I for each detector I.

While the foregoing establishes the form of the backscattered intensity response function, as a practical matter we must parameterize the function for *each* scenario in the SEM viewing window. This is because parameters m_I and b_I vary somewhat from crystal to crystal, due to the presence of nearby crystals that influence the path of backscattered electrons as they travel from crystal to detector. It is cumbersome, however, to use the stage-rotation method described above for each new scenario. Instead, we chose crystals that exhibited three smooth faceted surfaces of known orientation, and used backscattered intensities from a single stage orientation for calibration. For example, for crystal *2016-06-30_ice4_full2* displayed in Fig. 3.3a, we drew projected vectors $\vec{a}$, $\vec{b}$, and $\vec{c}$, and calculated surface normal vectors $\vec{n}_*$ and $\vec{n}_x$ of the corresponding prismatic facets. In addition, the normal vector to an adjacent pyramidal facet, designated $\vec{n}_+$, is obtained by rotating $\vec{n}_x$ by 28° along $\vec{b}$. Three backscattered intensities, obtained by averaging brightness values from rectangular segments on the corresponding facets, are also computed. This procedure yields three values of backscattered intensity as a function response variable, s_I, for each detector, from which parameters m_I and b_I may be analyzed by a best-fit least-squared criterion, as shown in Fig. 3.2b for crystal *2016-06-30_ice4_full2*. Parameterizations for this and other crystals are tabulated in Table S1 of Supplementary Information.

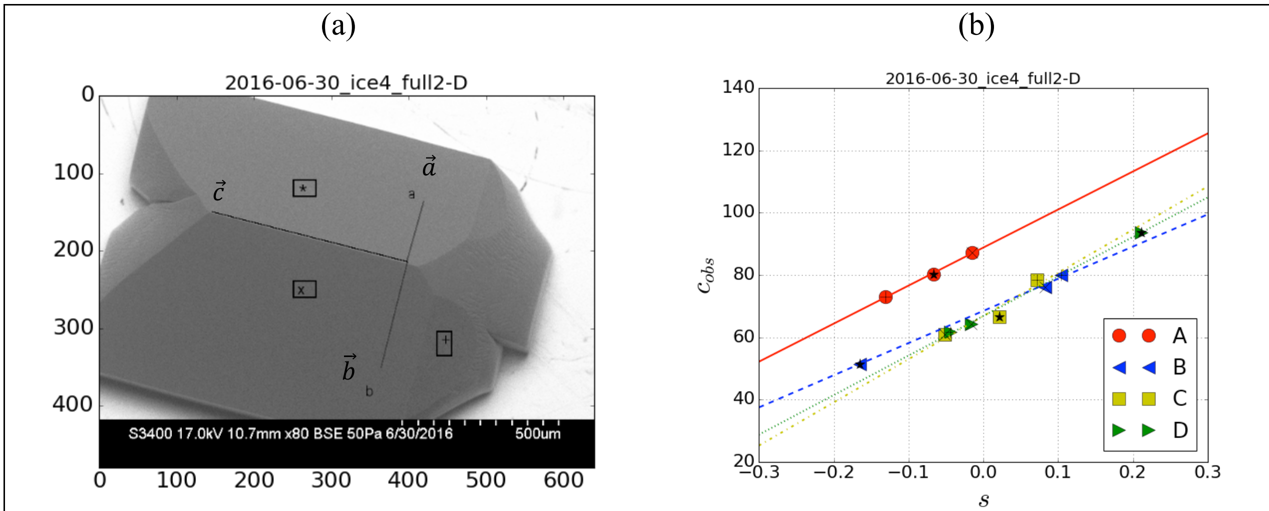

Figure 3.3. Response function calibration. (a) SEM image of crystal *2016-06-30_ice4*, grown and imaged at $-36°C$. Calibration areas are indicated in boxes: prismatic areas '*' and 'x', and pyramidal area '+'. Axes show crystal alignment. (b) Observed backscattered intensities, with symbols '*', 'x', and '+' referring to boxed areas in (a). Lines are based on a best-fit least-squared criterion for each detector.

3.2 Formulation of GNBF inversion for retrieving surface heights from SEM micrographs

With a parameterized response function in hand, the next step is to formulate an algorithm to retrieve surface heights from SEM images. We seek an algorithm that yields a global solution while minimizing the effects of noise. The algorithm applied here is Gauss-Newton in a Bayesian framework (GNBF inversion), which is designed to optimize such properties [*Rodgers*, 2000]. GNBF inversion is developed below in the context of Fig. 3.1b, a 3x3 height grid in which backscattered intensities are understood to originate from four triangular "pixels" (each received by four detectors). Generalization to larger image grids is straightforward. An analogous one-dimensional development is given in Appendix A2.

Surface heights displayed in Fig. 3.1b are specified by an 8×1 matrix as

$$\mathbf{Z} = \begin{bmatrix} Z[1] \\ \vdots \\ Z[8] \end{bmatrix}. \tag{3.3}$$

Normal surface vector components (in x- and y-directions) are specified by 4×1 matrices

$$\mathbf{N}_x = \begin{bmatrix} N_x[i] \\ \vdots \\ N_x[l] \end{bmatrix}, \quad \mathbf{N}_y = \begin{bmatrix} N_y[i] \\ \vdots \\ N_y[l] \end{bmatrix} \tag{3.4}$$

which are combined into a single 8×1 matrix

$$\mathbf{N} = \begin{bmatrix} \mathbf{N}_x \\ \mathbf{N}_y \end{bmatrix}. \tag{3.5}$$

Observed backscattered intensities at a given detector *I* are given by the 4×1 matrix

$$\mathbf{c}_I = \begin{bmatrix} c_I[i] \\ \vdots \\ c_I[l] \end{bmatrix} \tag{3.6}$$

which are combined (using four detectors) into the 16×1 matrix

$$\mathbf{c} = \begin{bmatrix} \mathbf{c}_A \\ \mathbf{c}_B \\ \mathbf{c}_C \\ \mathbf{c}_D \end{bmatrix}. \tag{3.7}$$

Next we define a 4×4 diagonal matrix that contains the dependence of the backscatter response function on x-direction gradients

$$\mathbf{K}_{I,x} = \begin{bmatrix} \left(\frac{\partial F[i]}{\partial N_x}\right)_{N_y} & 0 & 0 \\ 0 & \ddots & \vdots \\ 0 & \cdots & \left(\frac{\partial F_I[l]}{\partial N_x}\right)_{N_y} \end{bmatrix} \tag{3.8}$$

and y-direction gradients

$$\mathbf{K}_{I,y} = \begin{bmatrix} \left(\frac{\partial F[i]}{\partial N_y}\right)_{N_x} & 0 & 0 \\ 0 & \ddots & \vdots \\ 0 & \cdots & \left(\frac{\partial F[l]}{\partial N_y}\right)_{N_x} \end{bmatrix} \tag{3.9}$$

and combine them into a 4×8 matrix

$$\mathbf{K}_{xy} = \left[\mathbf{K}_{I,x}\ \mathbf{K}_{I,y}\right]. \tag{3.10}$$

Variations in the observed intensity at all four detectors can now be expressed as a function of variations in the surface normal x- and y-components according to

$$\delta\mathbf{c} = \mathbf{K}_{xy}\delta\mathbf{N}. \tag{3.11}$$

Surface normal components can be obtained from surface heights according to

$$\mathbf{N} = \mathbf{M}_{xy}\mathbf{Z} \tag{3.12}$$

where $\mathbf{M}_{xy}$ is defined by

$$\mathbf{M}_{xy} = \begin{bmatrix} \mathbf{M}_x \\ \mathbf{M}_y \end{bmatrix} \tag{3.13}$$

in which $\mathbf{M}_x$ and $\mathbf{M}_y$ are gradient operator matrices in the x- and y-directions; these are given explicitly for the one-dimensional case in Appendix A2. We next shift the variation operator (δ) to the right, giving

$$\delta\mathbf{c} = (\mathbf{K}_{xy}\mathbf{M}_{xy})\delta\mathbf{Z} \tag{3.14}$$

where the quantity in parentheses is a 16×8 matrix. It bears noting that this shifting is a key part of the development, as doing so builds continuity of the surface into the retrieval algorithm.

Equation 3.14 represents an overdetermined problem in which sixteen known backscattered intensities contained in **c** are available to infer eight unknown heights contained in **Z**. Larger surfaces are formulated in a similar fashion, but always in such a way that the number of observations (length of **c**) is greater the number of unknown heights (length of **Z**).

We are now prepared to apply GNBF inversion to the problem. Conventionally, the quantity in parenthesis in Eq. 3.14 is described as a kernel

$$\mathbf{K} = \mathbf{K}_{xy}\mathbf{M}_{xy} \tag{3.15}$$

so the variation matrix equation becomes

$$\delta\mathbf{c} = \mathbf{K}\delta\mathbf{Z}. \tag{3.16}$$

The solution is iterative, and can be developed by expressing the variation in surface heights as

$$\delta\mathbf{Z} = \mathbf{Z}_{n+1} - \mathbf{Z}_n \tag{3.17}$$

where $\mathbf{Z}_n$ is a previously-obtained (or initial) vector of surface heights, and $\mathbf{Z}_{n+1}$ is the result of the next iteration. Using $\mathbf{Z}_n$, we calculate $\mathbf{c}_n = \mathbf{F}_I(\mathbf{Z}_n)$ for each detector, and express the variation in **c** as

$$\delta\mathbf{c} = \mathbf{c}_{obs} - \mathbf{c}_n \tag{3.18}$$

where $\mathbf{c}_{obs}$ is a vector of observed backscattered intensities. The resulting GNBF inversion formula for iterating these solutions is given by

$$\mathbf{Z}_{n+1} = \mathbf{Z}_a + \left(\mathbf{S}_a^{-1} + \mathbf{K}'_n\mathbf{S}_e^{-1}\mathbf{K}_n\right)^{-1}\left[\mathbf{K}'_n\mathbf{S}_e^{-1}\left(\mathbf{c}_{obs} - \mathbf{c}_n + \mathbf{K}_n(\mathbf{Z}_n - \mathbf{Z}_a)\right)\right] \tag{3.19}$$

where $\mathbf{S}_a$ is a diagonal matrix whose elements equal the square of the estimated standard deviation in the heights, **Z**; we typically specify this standard deviation as ~10 μm in our retrievals. Similarly, $\mathbf{S}_e$ is a diagonal matrix whose elements equal the square of the estimated uncertainty in the observed backscattered intensity. We typically specify this uncertainty as ~2 %. (A sensitivity analysis studying the effect of varying $\boldsymbol{S}_a$ and $\boldsymbol{S}_e$ is described below, in Section 4.) We use a priori values $\mathbf{Z}_a = 0$, and an initial solution $\mathbf{Z}_{n=0} = 0$. Because Eq. 3.19 is applied iteratively, it is not necessary for the forward model, $\mathbf{F}_I(\mathbf{Z}_n)$, to be linear, but rather only that it be weakly nonlinear and characterized by an error contour surface with a single minimum. We find that only three iterations are needed for convergence in most cases.

In practice, application of the GNBF inversion algorithm is limited by the size of the kernel, **K**. The number of elements in **K** increases as the square of the number of pixels, which itself scales as the square of the length of a side of a roughly square subset (or "panel") of an SEM image. On a laptop computer, we find that GNBF inversion is limited to panels up to about 50×50 pixels. With the help of a graphical processing unit, we can increase this to panels of about 100×100 pixels. Analysis of larger subsets of a given SEM image is done by patching together GNBF-derived panels side by side, a composite reconstruction. Discontinuities in composite reconstructions, where panels are adjacent to one another, are therefore often evident.

GNBF inversion is validated by comparing retrieved surface angles of a smooth crystal to known crystal facet orientations. For crystal *2016-06-30_ice4*, for example, we retrieve the surface shown in Fig. 3.4. The retrieved angle between prismatic facets Pr1 and Pr2 is 52°, a 13% error from the presumed angle of 60°.

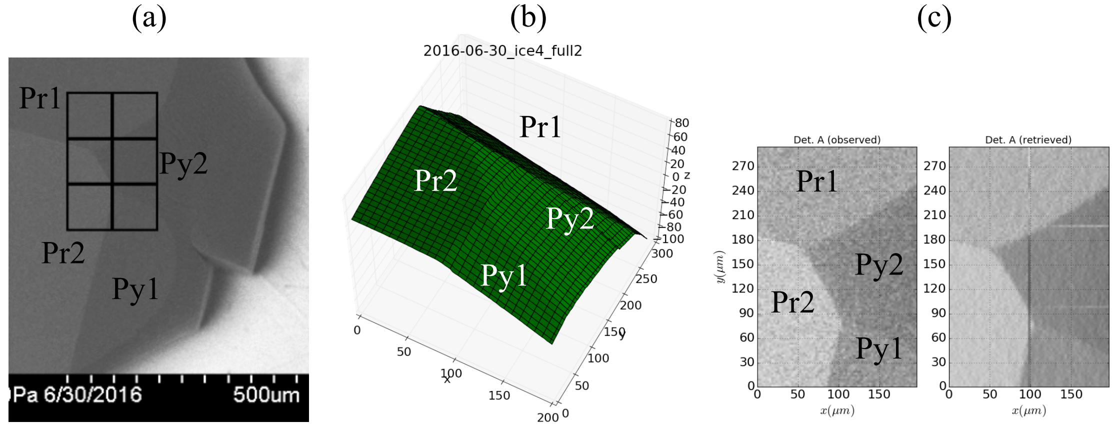

Figure 3.4. Retrieval validation. (a) SEM image of an expanded view of Crystal *2016-06-30_ice4*, grown and imaged at $-36°C$ showing a composite grid with prismatic (Pr1 and Pr2), pyramidal (Py1), and secondary pyramidal (Py2) facets annotated. (b) Retrieved surface height, with vertical scale exaggerated; the retrieved angle between Pr1 and Pr2 is 52°. (c) Comparison of observed and forward-modeled B-detector images of the grid. All distances are in micrometers. Related animation S1 is available in the Supplementary Information.

3.3 Calculation of roughness statistics

In previous work [*Pfalzgraff et al.*, 2010], the authors described a distinction between ice crystal roughness associated with *ablation* vs *growth*. Here we describe our efforts to quantify this distinction. Crystals were grown and calibrated (i.e., values of m_I and b_I were determined) at a temperature of -36 ℃ and a chamber pressure of 50 Pa. Growth scenarios presented below were obtained by monitoring crystals over a period of a few minutes as they continued to grow at temperatures below -33 ℃. Ablation scenarios were similarly obtained, but by raising the temperature of the Peltier cooling element to -32 ℃, which is just above the equilibrium temperature, or higher. Surfaces were then retrieved using GNBF inversion using values of m_I and b_I obtained for that crystal, and characterized in terms of roughness according to the methods described in Section 2.

Figure 3.5 shows growth roughness on crystal *2016-06-30_ice4* after several minutes at a temperature of −33 °C. An SEM image from detector A is shown in Fig. 3.5a, in which azimuthally anisotropic roughness can be seen as near-vertical trenches in the image. A horizontal intersection between two prismatic facets occurs in this field of view, but it is scarcely visible by the A detector (it is better seen by the B and D detectors, because of their orientation below and above this intersection). Regions to be reconstructed are indicated by the boxed segments. The A- and B-detector grids shown in Fig. 3.5b illustrate the different perspectives provided by each backscatter detector. The A-detector highlights the trench-like roughness feature, whereas the B-detector highlights the facet intersection. Figure 3.5c shows the surface heights retrieved using GNBF inversion, in which both the facet edge and the roughness are evident. The average roughness of this area is $\langle r \rangle = 0.01$ (equivalent to $\sigma = 0.15$). Figure 3.5d shows that a Cox-Munk distribution ($\eta = 1$) provides the best fit to the observed roughness distribution.

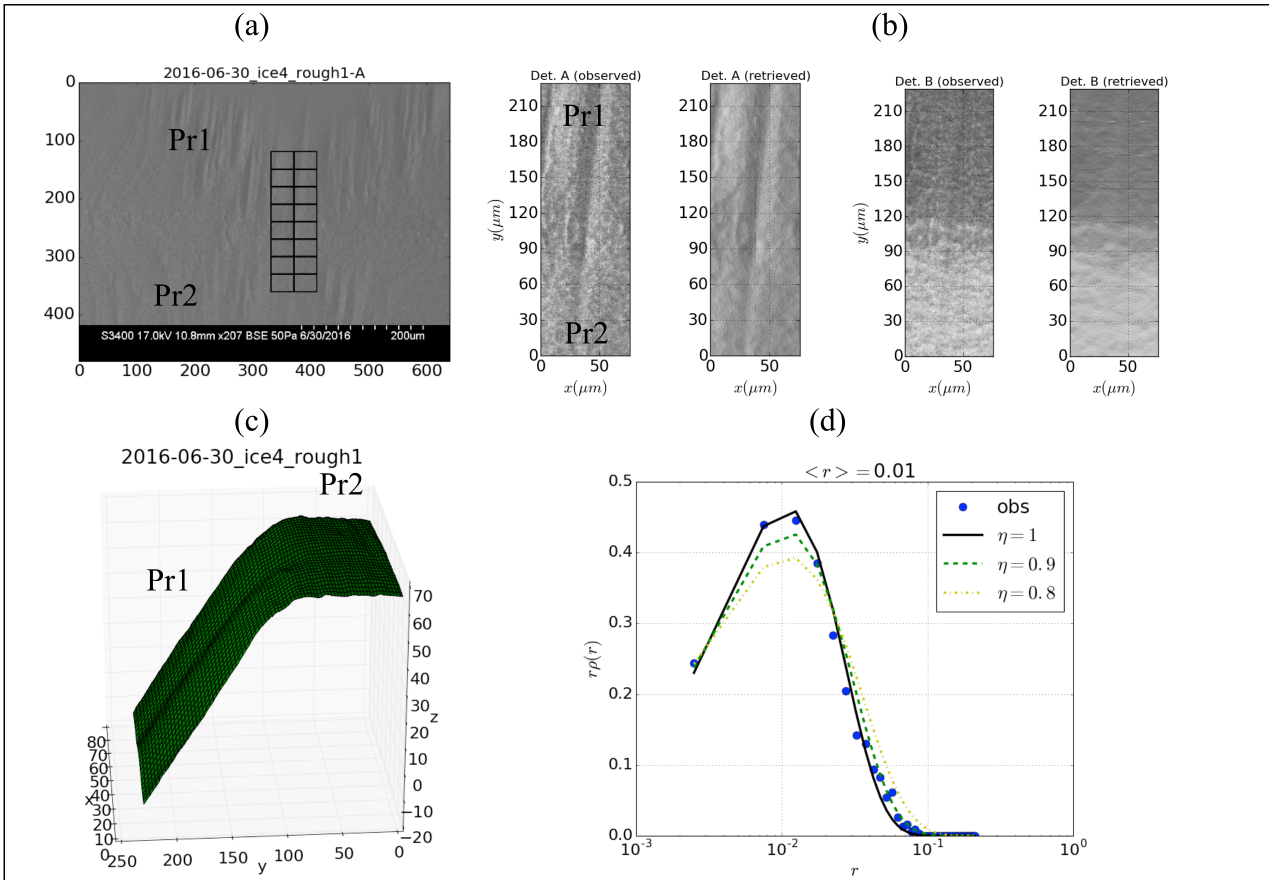

Figure 3.5. Quantification of ablation roughness on crystal *2016-06-30_ice4*, roughening case 4.1.4. This crystal is the same as that appearing in Fig. 3.4, but after roughening was induced by raising the temperature to $-33°C$. (a) SEM image of the crystal after roughening, expanded around the intersection between prismatic facets. The retrieval region is highlighted. (b) Observed and forward-modeled A- and B-detector grids. (c) Retrieved surface heights in the retrieval grid, vertical scale exaggerated. (d) Roughness distributions. Markers show PDFs of facet Pr1 of the grid shown in (a) (top six panels). Lines show Weibull distributions. Related animations S2 and S3 are available in the Supplementary Information.

We next examine a second case of growth roughness, on crystal *2016-06-30_ice5*, also at −33 °C. Figure 3.6a shows an SEM image of the facet surface, with the region to be reconstructed indicated by boxes. Figure 3.6b shows an expanded view of the retrieved region, paired with the result of a forward model calculation based on the retrieved surface.

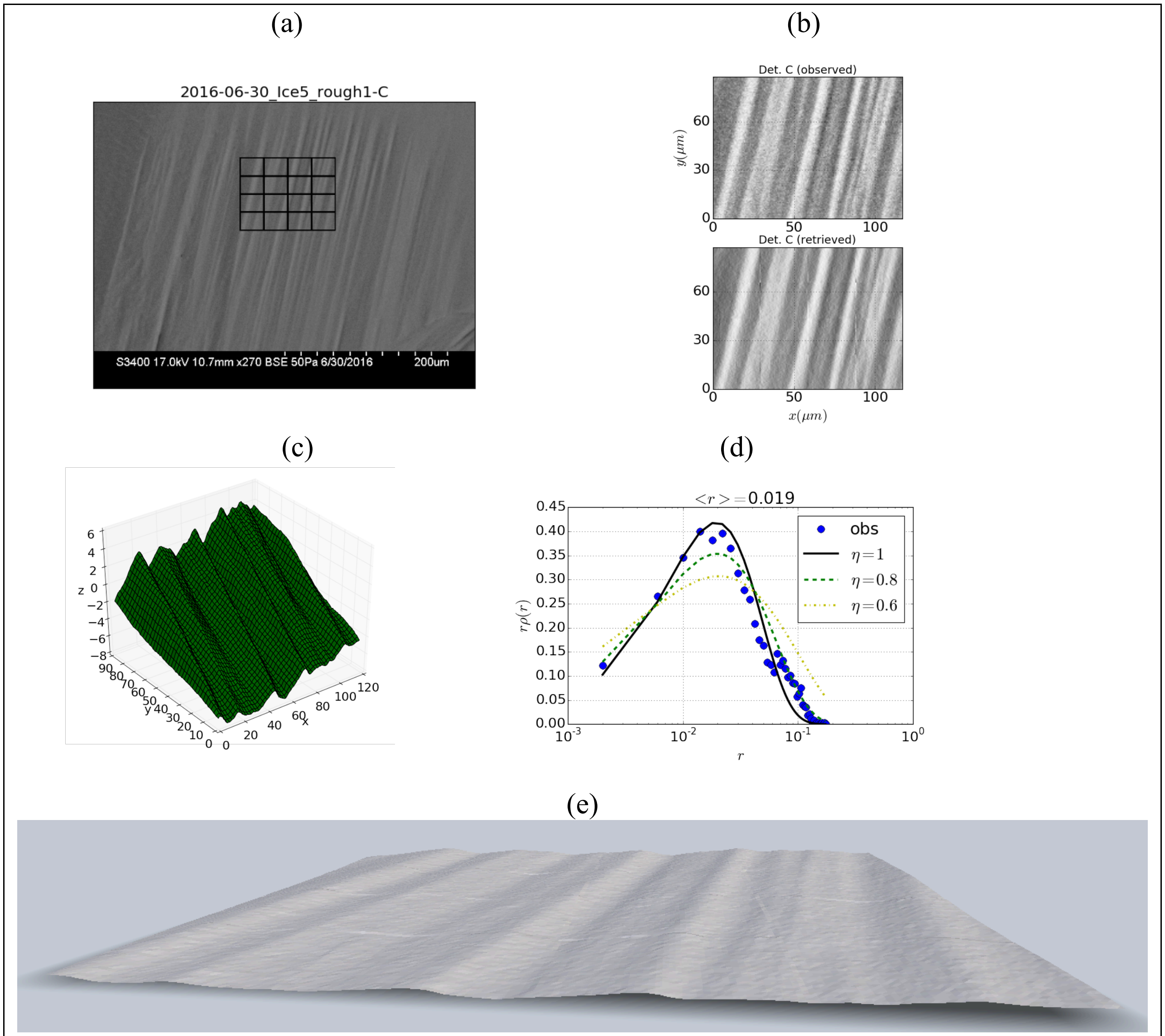

Figure 3.6. Quantification of growth roughness on a prismatic facet of crystal *2016-06-30_ice5*, at −33 °C. (a) SEM image with the retrieval region highlighted. (b) Observed and forward-modeled images for detector C. (c) Retrieved surface heights with vertical scale exaggerated. (d) Roughness distributions. Lines show Weibull distributions. (e) Retrieved surface with equal vertical and horizontal scales.

The reconstructed surface itself is shown in Fig. 3.6c, with the vertical scale exaggerated to highlight roughness features. Figure 3.6d shows experimental and Weibull PDFs. We find an average roughness of $\langle r \rangle = .019$ ($\sigma = .20$), which is among the larger values we observe for growth roughness. A slight shoulder peak is evident at $r = 0.065$, which corresponds to a tilt angle of approximately 20°. A Cox-Munk PDF ($\eta = 1$) appears to fit the distribution better to the left of this shoulder, while a shape parameter of $\eta = 0.8$ does better to the right. Figure 3.6e depicts the reconstructed surface with equal vertical and horizontal scales.

We present in Fig. 3.7 our analysis of another ice crystal, this one growing at -36 ℃. Figure 3.7a suggests that a pyramidal facet located in the upper portion of the image is smooth, while the prismatic facet exhibits significant growth roughness. The reconstructed region includes the roughest part of the prismatic facet, with results shown in Fig. 3.7b. As expected, retrieved roughness features are clearly azimuthally anisotropic, although these features are less ordered than in the previous example. Figure 3.7c shows the corresponding roughness distribution (prismatic facet only), characterized by $\langle r \rangle = 0.033$ ($\sigma = 0.27$). The shape of this distribution is best fit by $\eta = 0.9$, with a shoulder once again evident. Figure 3.7d presents the three-dimensional surface with equal vertical and horizontal scales.

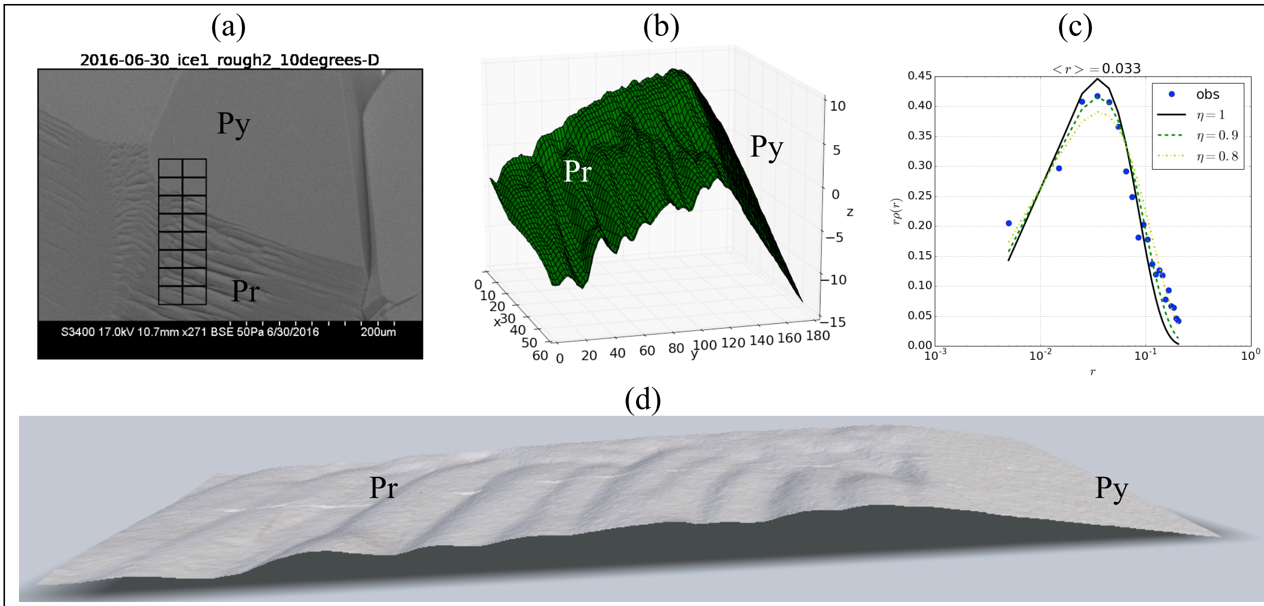

Figure 3.7. Quantification of growth roughness of crystal *2016-06-30_ice1*, roughness case 1.2. growing at -36 ℃. (a) SEM image of an intersection between the pyramidal (Py) and prismatic (Pr) facets. The retrieval region is highlighted. (b) Retrieved surface heights, vertical scale exaggerated. (c) Observed and Weibull PDFs characterizing the five lowest panels in the right-hand side of the grid shown in (a). (d) Retrieved surface with equal vertical and horizontal scales.

Figure 3.8 displays results for the same crystal as in Fig. 3.7, but focusing on a different region of the prismatic facet. In terms of the symmetry of the roughening, much of the same conclusions hold for this roughening, although the depth of the roughening appears greater here (Fig. 3.8b). As Fig. 3.8c demonstrates, this region is distinguished by a marked bimodality in the shape of the roughness distribution appears: the pronounced shoulder peak is present at $r = 0.15$, equivalent to a tilt angle of approximately 30°.

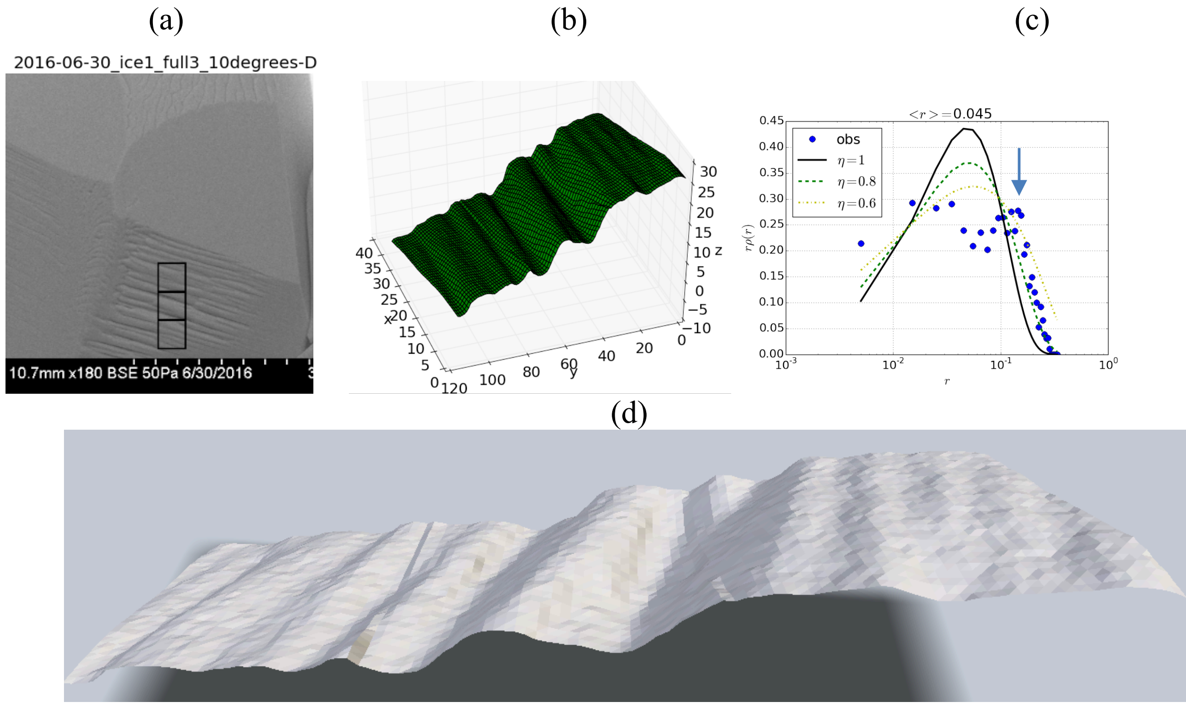

Figure 3.8. Quantification of growth roughness of crystal *2016-06-30_ice1*, $T = -36$ °C. (a) SEM image with the retrieval region highlighted. (b) Surface heights plotted with vertical scale exaggerated. (c) Roughness statistics for the retrieval region. The arrow points to roughness value corresponding to a zenith angle of 30°. (d) Retrieved surface with equal horizontal and vertical scales.

Figure 3.9 explores roughness on a crystal that was first ablated by slowly reducing temperature to −28.5 °C, then regrown at −36 °C. The retrieval region, highlighted in Fig. 3.9a, is located where the pyramidal and rounded facet were evident while the crystal was growing, but after ablation and regrowth it cannot be assigned to any particular facet category. Figure 3.9b shows the reconstructed surface, in which the roughness appears azimuthally isotropic. Figure 3.9c shows PDFs of this region along with Weibull functions. This case, and similar ones presented in Figs. S1 and S2 in Supplementary Information, indicate that isotropic roughness is best described by a Cox-Munk distribution.

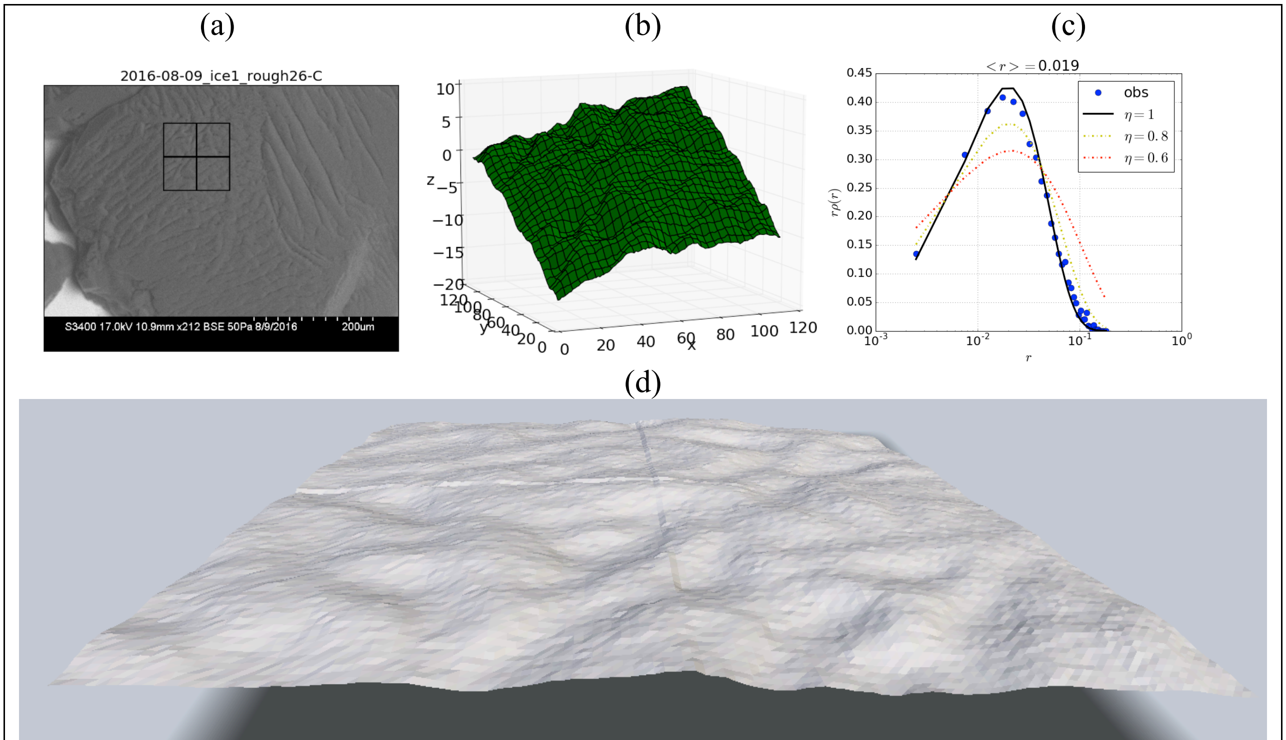

Figure 3.9. Quantification of isotropic roughness at −36 °C (after ablation). (b) Retrieved surface heights plotted with vertical scale exaggerated. (c) Roughness statistics for the retrieval region. (d) Retrieved surface with equal vertical and horizontal scales.

Figure 3.10 shows a series of surfaces captured at approximately 1 °C intervals between −33 °C and −28.5 °C. As the temperature increases into the ablation regime, roughness features grow deeper and wider. Between the temperatures of −33 °C and −31 °C, this causes an increase in $\langle r \rangle$ from 0.011 to 0.031. Above −29.5 °C, we observe a slight *reduction* in roughness, to $\langle r \rangle = 0.028$ at −28.5 °C. Analysis of the lower facet of this crystal over approximately the same temperature range is presented in Fig. S3 of Supplementary Information, with similar results.

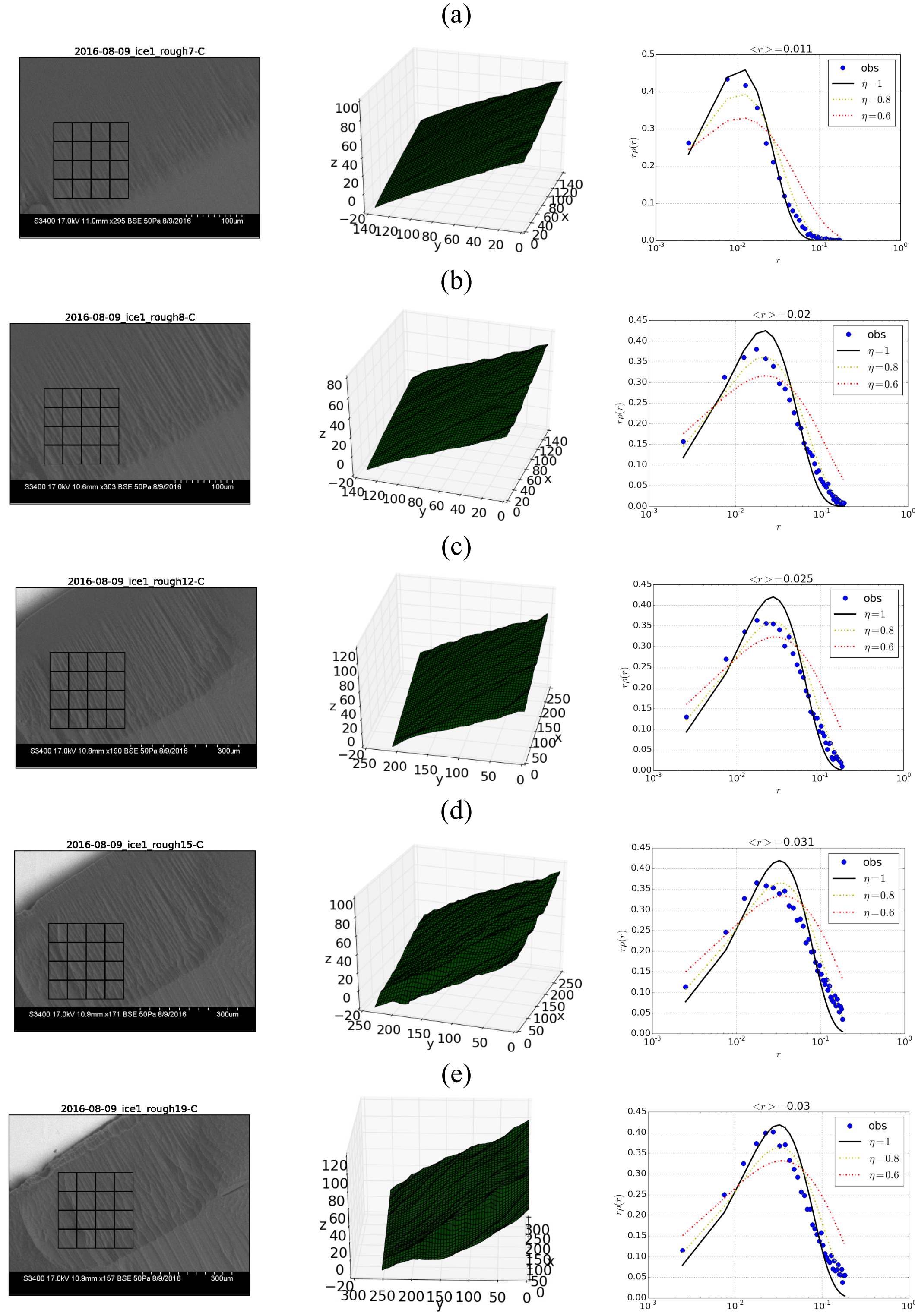

Figure 3.10. Quantification of roughness on an ablating prismatic facet. (a) T = −33 °C; (b) T = −32 °C; (c) T = −32 °C; (d) T = −31 °C; and (e) T = −29.5 °C.

381

4 Discussion

4.1 Sensitivity of retrieval to GNBF parameters

Variances in the a priori heights, $\boldsymbol{S}_a$, and the variances in the measured backscattered intensities, $\boldsymbol{S}_e$, must be specified as part of the GNBF inversion. A sensitivity study was performed to estimate the influence of $\boldsymbol{S}_a$ and $\boldsymbol{S}_e$ on retrieved roughness statistics, as follows. From an SEM image, surface heights were retrieved for three different $\boldsymbol{S}_e$ matrices. These were based on standard deviations of 0.030, 2.2, and 7.1 BIU. (Recall that the matrices $\boldsymbol{S}_a$ and $\boldsymbol{S}_e$ are diagonal with diagonal elements corresponding to the square of the standard deviation in BIU, for $\boldsymbol{S}_e$, and the square of the uncertainty in the a priori heights, for $\boldsymbol{S}_a$). Retrievals were performed for $\boldsymbol{S}_a$ based on standard deviations in heights of 0.70, 3.2, and 17 μm. The maximum difference in retrieved surface heights between each retrieval for this crystal case was 0.2 μm and the roughness statistics for $\langle r \rangle$ agreed to two significant figures across all retrievals. Observations of other cases showed similar robustness to small variations of $\boldsymbol{S}_a$ and $\boldsymbol{S}_e$.

We also investigated the sensitivity of roughness to the grid size of retrieved segments. Two retrievals of an identical region on the crystal *2016-06-30_ice4* were performed, one using a single 90x90 grid and the other using nine 30x30 grids. The resulting mean roughness values differed on the order of 5%, with $\langle r \rangle = 0.020$ and 0.021, respectively.

An important motivation for using the GNBF formalism for the inverse retrieval is that the retrieval finds the *optimal* solution within the solution region characterized by the uncertainties. This framework avoids the extreme sensitivity to noise that is "a common feature of exact solutions to retrieval problems" [*Rodgers*, 2000]. This is particularly important for acquiring roughness statistics because small-scale noise will increase $\langle r \rangle$. Qualitative inspection of results shows that forward-modeled images do indeed exhibit reduced small-scale pixel-scale variation in backscatter intensity compared to observations, as desired.

4.2 Variation in response function parameters

As described in Section 3, we calibrated the backscatter response parameters m_I and b_I for each detector and crystal, and used those parameters to retrieve surface heights of those crystals after roughening. We believe these parameters vary from detector to detector because of inherent differences in detector sensitivity. For example, Detector A generally records brighter backscattered intensities than the other detectors. It is unclear why, however, the backscatter response parameters should vary from scenario to scenario (i.e., from crystal to crystal). We speculate that detector sensitivity depends on the proximity of other ice crystals, which may create a lensing effect due to local variations in water vapor concentration. To minimize this possibility, we selected relatively isolated ice crystals for our analysis.

4.3 Trends from roughness statistics

Roughness statistics are summarized in Table 1. The naming convention for cases is as follows: the first number refers to crystal identity, second refers to the particular roughening scenario, and the third differentiates between different analyses of the same image. Regarding the degree of roughening, we see that values of $\langle r \rangle$ reach as high as 0.045 ($\sigma = 0.31$). Regarding the shape parameter, we see that *ablation* roughening is best described by $\eta = 0.8$, *azimuthally isotropic* roughening is characterized by $\eta = 1$, and *azimuthally anisotropic* roughening in the growth regime ranges between $\eta = 0.8$ and $\eta = 1$. These observations suggest that remote sensing results may contain more facet-specific information, and information that allows one to distinguish growth from ablation conditions, than has been previously appreciated.

Table 1. Roughness statistics for all crystals. Crystals at or below −33°C are in the growth regime, and crystals above −33°C are in the ablation regime.

Crystal	Roughness case	Temperature (℃)	$\langle r \rangle$	σ	η
2016-08-26_ice1	1.3	−39	.005	.097	1.0
2016-08-26_ice1	1.4	−39	.005	.101	1.0
2016-08-26_ice2	2.6	−39	.018	.19	0.8
2016-08-26_ice3	3.2	−39	.018	0.2	0.8
2016-06-30_ice1	1.1.2	−36	.017	.188	0.8
2016-06-30_ice1	1.2.1	−36	.033	.266	1.0
2016-06-30_ice1	1.5	−36	.045	.31	n/a
2016-06-30_ice1	1.4	−33	.017	.185	0.8
2016-06-30_ice3	3.1.1	−33	.008	.123	1.0
2016-06-30_ice4	4.1.4	−33	.011	.145	0.9
2016-06-30_ice5	5.1	−33	.019	.20	1.0
2016-06-30_ice8	8.1	−33	.005	.101	1.0
2016-08-09_ice1	1.7	−33	.011	.15	1.0
2016-08-09_ice1	1.8	−33	.020	.21	0.9
2016-08-09_ice1	1.11	−32	.025	.23	0.8
2016-08-09_ice1	1.12	−32	.025	.24	0.8
2016-08-09_ice1	1.14	−32	.018	.19	0.8
2016-08-09_ice1	1.15	−31	.031	.26	0.8
2016-08-09_ice1	1.17	−31	.020	.21	0.8
2016-08-09_ice1	1.19	−29.5	.030	.25	1.0
2016-08-09_ice1	1.21	−29.5	.022	.22	0.8
2016-08-09_ice1	1.24	−28.5	.028	.25	0.9
2016-08-09_ice1	1.25	−28.5	.015	.17	0.8

4.4 Relationship to previous results

Our SEM results compare favorably to nephelometry results for natural ice crystals observed at South Pole Station [*Shcherbakov et al.*, 2006a, 2006b], which report a similar degree of roughness as we retrieved, with σ in the range of 0.05-0.25. However, that study indicated values of η between 0.73 and 0.77, lower than our values of 0.8 and above. Because our study focuses primarily on prismatic facets, the disagreement may be due to roughness effects from crystal regions not studied here, such as basal or rounded facets. It is also possible that remote-sensing retrievals interpret bimodal distributions such as that appearing in Fig. 3.6c for Weibull distributions with small η. More research into these possibilities is required to resolve these questions.

A distinct advantage of the present method over the method based on prismatic facet intersections described previously ([*Neshyba et al.*, 2013]) is that it is less restrictive: one does not need to find cases in which roughness appears at these intersections, nor does one need to assume that such roughening is representative of facet interiors. Indeed, Magee et al. [2014] found that it was rare to find well-resolved roughness that intersected facet edges, and therefore could not obtain quantitative data on much of the roughness they observed. A second advantage is that the present method, in retrieving heights as a function of two horizontal dimensions, provides far more data, and therefore greatly increases confidence in the statistical properties of roughening.

Magee et al. [2014] present evidence that roughness occurs on scales as small as the sub-micron level, which is below the imaging resolution attainable by the SEM used for our study. Further study is necessary to elucidate the relative importance of mesoscale versus sub-micron scale roughness in relation to optical scattering.

The method of retrieval via GNBF inversion developed in this paper can be applied to other materials for which quantitative data concerning surface structure is of interest. However, several conditions must be met by the material in question: it must be homogeneous, such that all variation in backscatter intensity is due to surface tilt, and it must be continuous so that gradients may be calculated at all points. The first condition may be circumvented by coating techniques such as sputtering with gold-palladium, if the desired features are large enough that they will not be obscured by the coating.

5 Conclusions

We have presented a method for retrieving quantitative, three-dimensional surface morphology of ice from SEM images. A key development is a novel functional form for backscattered electron density as a function of ice facet orientation. In combination with Gauss-Newton inversion within a Bayesian framework, the method permits construction of three-dimensional representations of the surface of rough ice at approximately micrometer resolution. Probability densities of surface roughness derived from these surfaces indicate values of $\langle r \rangle$ as high as .045, and values of η ranging from 0.8 to 1.0. As *growth* roughening on prismatic facets becomes more pronounced, while lower values of η provide an approximate match to observations, it is clear that the Weibull form is qualitatively wrong: instead, a bimodal distribution appears, which cannot be described by the Weibull form. As *ablation* roughening becomes more pronounced, agreement between observed and best-fit Weibull distributions also deteriorates, but no obvious pattern is discernable in the discrepancy. We also find that $\langle r \rangle$ increases with higher temperature, but only to a point; at yet higher temperatures, we find $\langle r \rangle$ remains about the same. Altogether, these results suggest that roughening characteristics obtained by remote sensing of atmospheric ice clouds could be a richer source of information than has previously been appreciated.

Acknowledgements

S.N. was supported by NSF grant award CHE-1306366 for this work, and acknowledges support from a University of Puget Sound Lantz Senior Sabbatical Fellowship and the Fulbright

Scholar program. N.B. and E.S. acknowledge support from the University of Puget Sound. P.M.R. received support from Consejo Nacional de Ciencia y Tecnologia CONICYT- Anillos, Preis ACT 1410 and FONDECYT Regular 1161460. Computer codes implementing the continuum model are available at https://github.com/sneshyba/ice3. There are no data sharing issues since all numerical information is provided in figures and tables in this paper and in an SI file; the latter contains three figures, one table, and two animations.

Appendix A1. Solving for surface normals

In reference to Fig. 3.2 or 3.3, the vectors are drawn in the x-y plane, and the following conditions are used to solve for their missing z-component:

$$\vec{a} \cdot \vec{c} = 0 \tag{A1.1}$$
$$\vec{b} \cdot \vec{c} = 0 \tag{A1.2}$$
$$\vec{a} \cdot \vec{b} = -\frac{1}{2}|a||b| \tag{A1.3}$$
$$a_x^2 + a_y^2 + a_z^2 = |a|^2 \tag{A1.4}$$
$$b_x^2 + b_y^2 + b_z^2 = |b|^2 \tag{A1.5}$$
$$c_x^2 + c_y^2 + c_z^2 = |c|^2 \tag{A1.6}$$

Equations A1.1- A1.3 are consequences of the crystal geometry: the prismatic-prismatic edge ($\vec{c}$) must be perpendicular to the prismatic-pyramidal edges ($\vec{a}$ and $\vec{b}$) and the internal angle between the prismatic facets (*a* and *b*) must be 120°. Equations A1.4- A1.6 establish that each vector's components must correctly reproduce the magnitude of the vector. These conditions do not produce a single unique solution, so we must select the physically reasonable condition by requiring that all magnitudes be positive, and the *z*-component of $\vec{b}$ be physically correct (e.g., negative when the *b* facet is tilted downward). Surface normal vectors for the * and + facets are calculated by

$$\vec{n}_* = \vec{a} \times \vec{c} \tag{A1.7}$$
$$\vec{n}_+ = \vec{b} \times \vec{c} \tag{A1.8}$$

Appendix A2. GNBF inversion in one dimension

We begin with the formalism associated with an idealized one-dimensional crystal, as displayed in Fig. A.1. Here we have three surface heights, labeled *1-3*, and two microsurfaces adjoining them (each corresponding to a pixel in an SEM micrograph), labeled *i* and *j*. Normal vectors to these microsurfaces are defined to have components ($N_x[i]$,1) and ($N_x[j]$,1).

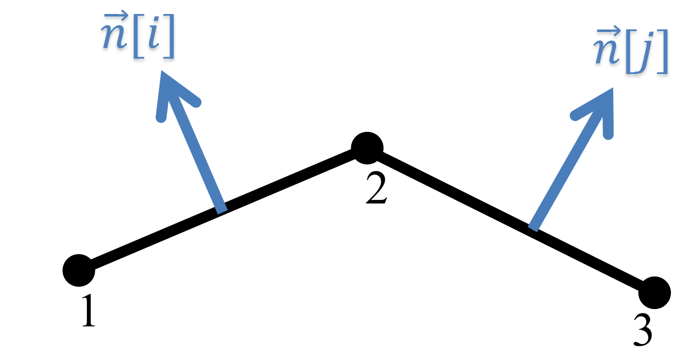

Figure A.1 Geometry of a one-dimensional retrieval grid. Normal vectors have components $(N_x, 1)$.

The three heights can be collected in a 3×1 matrix as

$$\mathbf{Z} = \begin{bmatrix} \mathrm{Z}[1] \\ \mathrm{Z}[2] \\ \mathrm{Z}[3] \end{bmatrix}. \tag{A2.1}$$

The two microsurfaces have normal vector x-components and detector intensities similarly specified, as 2×1 matrices

$$\mathbf{N}_x = \begin{bmatrix} N_x[i] \\ N_x[j] \end{bmatrix} \tag{A2.2}$$

and

$$\mathbf{c}_\mathrm{I} = \begin{bmatrix} c_I[i] \\ c_I[j] \end{bmatrix}. \tag{A2.3}$$

where I stands for one of the detectors A-D. A small variation in the gradient gives rise to a variation in this detector intensity that can be expressed in matrix form as

$$\delta \mathbf{c}_I = \mathbf{K}_{I,x} \delta \mathbf{N}_x. \tag{A2.4}$$

where we have defined the 2×2 diagonal matrix

$$\mathbf{K}_{I,x} = \begin{bmatrix} \frac{\partial F_I[i]}{\partial N_x} & 0 \\ 0 & \frac{\partial F_I[j]}{\partial N_x} \end{bmatrix}. \tag{A2.5}$$

Thus we have an inversion problem in which the matrix $\mathbf{K}_{I,x}$ must be inverted (or an equivalent procedure) in order to convert variations in observed backscattered intensities into variations in gradients. Our objective is a surface, **Z**, however. It is preferable, therefore, to cast the inversion problem in terms of an unknown surface directly. To do so, we relate normal vector x-components to surface heights according to

$$\mathbf{N}_x = \mathbf{M}_x\mathbf{Z} \tag{A2.6}$$

where $\mathbf{M}_x$ is a matrix corresponding to the gradient operator,

$$\mathbf{M}_x = \begin{bmatrix} -1 & 1 & 0 \\ 0 & -1 & 1 \end{bmatrix}. \tag{A2.7}$$

so that Eq. A2.4 can be written

$$\delta\mathbf{c}_I = \mathbf{K}_{I,x}\delta(\mathbf{M}_x\mathbf{Z}). \tag{A2.8}$$

Now we reposition the variation operator (δ) to the right

$$\delta\mathbf{M}_x(\dots) \rightarrow \mathbf{M}_x\delta(\dots) \tag{A2.9}$$

which converts the object of variation from gradients to surface heights. This yields

$$\delta\mathbf{c}_I = (\mathbf{K}_{I,x}\mathbf{M}_x)\delta\mathbf{Z} \tag{A2.10}$$

The elements in the quantity in parentheses can be computed using the forward model, F_I. Solution of this equation is underdetermined, however, because we wish to obtain three unknown surface heights (contained in $\mathbf{Z}$) from two known observed backscattered intensities (contained in $\mathbf{c}_I$). This deficiency can be remedied by the use of two detectors, *A* and *B*, forming the 4×2 matrix

$$\mathbf{K}_x = \begin{bmatrix} \mathbf{K}_{A,x} \\ \mathbf{K}_{B,x} \end{bmatrix}, \tag{A2.11}$$

We also define a matrix of observed backscattered intensities that includes detectors *A* and *B*,

$$\mathbf{c} = \begin{bmatrix} \mathbf{c}_A \\ \mathbf{c}_B \end{bmatrix} \tag{A2.12}$$

in which case the variation equation is written

$$\delta\mathbf{c} = (\mathbf{K}_x\mathbf{M}_x)\delta\mathbf{Z} \textit{ (1-d surface)} \tag{A2.13}$$

where the quantity in parentheses is a 4×3 matrix. This equation therefore represents an overdetermined problem in which four known backscattered intensities (contained in $\mathbf{c}$) are available to infer three unknown heights (contained in $\mathbf{Z}$). Equation A2.13 has the same form as Eq. 3.14 in Section 3, and can be developed to apply GNBF inversion in a similar way.

References

Bancroft, L., K. Boaggio, K. Hurler, M. Bandamede, and N. Magee (2016), Comparative analysis of lab-grown ice crystals by cryo-scanning electron microscopy, Manchester.

Baran, A. J. (2009), A review of the light scattering properties of cirrus, *J. Quant. Spectrosc. Radiat. Transf.*, *110*(14–16), 1239–1260.

Baran, A. J. (2012), From the single-scattering properties of ice crystals to climate prediction: A way forward, *Atmospheric Res.*, *112*, 45–69, doi:10.1016/j.atmosres.2012.04.010.

Baran, A. J. (2015), On the relationship between the scattering phase function of cirrus and the atmospheric state, *Atmospheric Chem. Phys.*, doi:10.5194/acp-15-1105-2015.

Blinn, J. F. (1977), Models of light reflection for computer synthesized pictures, *SIGGRAPH Comput Graph*, *11*(2), 192–198, doi:10.1145/965141.563893.

van Diedenhoven, B., A. S. Ackerman, A. M. Fridlind, and B. Cairns (2016), On Averaging Aspect Ratios and Distortion Parameters over Ice Crystal Population Ensembles for Estimating Effective Scattering Asymmetry Parameters, *J. Atmospheric Sci.*, *73*(2), 775–787.

Geogdzhayev, I., and B. van Diedenhoven (2016), The effect of roughness model on scattering properties of ice crystals, *J. Quant. Spectrosc. Radiat. Transf.*, *178*, 134–141, doi:10.1016/j.jqsrt.2016.03.001.

Hioki, S., P. Yang, B. A. Baum, S. Platnick, K. G. Meyer, M. D. King, and J. Riedi (2016), Degree of ice particle surface roughness inferred from polarimetric observations, *Atmospheric Chem. Phys.*, *16*(12), 7545–7558, doi:10.5194/acp-16-7545-2016.

Lynch, D. K. (2002), *Cirrus*, Oxford University Press, New York.

Magee, N. (2015), 3D Micro-topography of Transferred Laboratory and Natural Ice Crystal Surfaces Imaged by Cryo and Environmental Scanning Electron Microscopy, in *2015 AGU Fall Meeting*, Agu.

Magee, N. B., A. Miller, M. Amaral, and A. Cumiskey (2014), Mesoscopic surface roughness of ice crystals pervasive across a wide range of ice crystal conditions, *Atmos Chem Phys*, *14*(22), 12357–12371, doi:10.5194/acp-14-12357-2014.

Neshyba, S. P., B. Lowen, M. Benning, A. Lawson, and P. M. Rowe (2013), Roughness metrics of prismatic facets of ice, *J. Geophys. Res. Atmospheres*, *118*(8), 3309–3318, doi:10.1002/jgrd.50357.

Pfalzgraff, W. C., R. M. Hulscher, and S. P. Neshyba (2010), Scanning electron microscopy and molecular dynamics of surfaces of growing and ablating hexagonal ice crystals, *Atmos Chem Phys*, *10*(6), 2927–2935, doi:10.5194/acp-10-2927-2010.

Rodgers, C. D. (2000), *Inverse methods for atmospheric sounding: theory and practice*, World scientific.

Shcherbakov, V., J. F. Gayet, O. Jourdan, J. Ström, and A. Minikin (2006a), Light scattering by single ice crystals of cirrus clouds, *Geophys. Res. Lett.*, *33*(15), L15809, doi:10.1029/2006GL026055.

Shcherbakov, V., J. F. Gayet, B. Baker, and P. Lawson (2006b), Light scattering by single natural ice crystals, *J. Atmospheric Sci.*, *63*(5), 1513–1525.

Stephens, G., S. Tsay, P. W. Stackhouse, and P. J. Flatau (1990), The relevance of the microphysical and radiative properties of cirrus clouds to climate and climatic feedback, *J. Atmospheric Sci.*, *47*(14), 1742–1753.

Ulanowski, Z., P. H. Kaye, E. Hirst, R. S. Greenaway, R. J. Cotton, E. Hesse, and C. T. Collier (2014), Incidence of rough and irregular atmospheric ice particles from Small Ice Detector 3 measurements, *Atmos Chem Phys*, *14*(3), 1649–1662, doi:10.5194/acp-14-1649-2014.

Xie, Y. (2012), The effect of ice crystal surface roughness on the retrieval of ice cloud microphysical and optical properties, Ph.D Dissertation, Texas A&M University.